IET Radar, Sonar & Navigation

Research Article

IET Journals
The Institution of Engineering and Technology

Comparison of SBR and MLFMM techniques for the computation of RCS of a fighter aircraft

ISSN 1751-8784
Received on 13th February 2019
Revised 10th May 2019
Accepted on 10th June 2019
E-First on 31st July 2019
doi: 10.1049/iet-rsn.2019.0070
www.ietdl.org

Ahmad Bilal[1] ✉, *Syed Muhammad Hamza*[1], *Ziauddin Taj*[2], *Shuaib Salamat*[2]

[1]*Department of Avionics Engineering, Air University PAC Campus, Kamra, Pakistan*
[2]*Department of Aerospace Engineering, Air University PAC Campus, Kamra, Pakistan*
✉ *E-mail: ahmadbilal@aerospace.pk*

Abstract: In this work, an extensive correlation between two commonly used radar cross-section (RCS) computation techniques, i.e. shooting and bouncing rays (SBR) and multilevel fast multipole method (MLFMM), is performed. Numerical results are compared with the measured data, obtained from an anechoic chamber, for a 1:8 scaled down model of a fighter aircraft. It is ascertained that the SBR method, notwithstanding its numerical simplicity, can provide qualitatively similar and reasonably accurate RCS results for an object of varying complexity.

1 Introduction

The advent of high performance computing (HPC) has significantly improved the ability to perform complex electromagnetic calculations promptly and accurately [1–3]. These simulations become more intricate when computing radar cross-section (RCS) of electrically large objects such as aircrafts, ships, and missiles, as it involves the full wave solution of the electromagnetic field integral [4–6]. To cater for such complexities, various algorithms have been developed over a period of time including finite-difference time-domain method [7], method of moments (MoMs) [5], physical optics (PO) [8], and shooting and bouncing rays (SBR) [9]. The choice of these algorithms depends upon few major factors such as target size relative to the radar wavelength, accuracy, and computational time.

MoM is an industry standard technique to compute the RCS and is incorporated by most of the electromagnetic solvers such as High Frequency Structural Simulator and CST Microwave Studio. MoM is applied in the Rayleigh and resonance region where the target size is $<\sim 10$ wavelengths [5]. On the other hand, for electrically large structures, MoM is usually avoided because of the substantial amount of processing power and memory required to handle a very refined mesh. To offset the inherent computational cost and memory requirements of MoM, multi-level adaptive cross approximation matrix compression, and multi-level fast multipole method (MLFMM) techniques are used to speed up the convergence [6, 10]. In this work, we use MLFMM since it is more suitable, in terms of memory, for the simulation of a large number of unknown surfaces [11].

However, to reduce the simulation time while maintaining reasonable accuracy, the SBR method, a technique which computes the RCS in the optical regime, has long been developed [12]. SBR employs a combination of geometric optics (GO) and PO techniques, and by combining both methodologies, SBR performs calculations by originating numerous optical ray tubes [13, 14]. Each corner ray of the ray tube is traced using GO where the wave front parameters such as the magnitude, phase, and direction are superimposed on the rays. The wave propagation is modelled as the refraction, reflection, and divergence of optical rays. As each ray encounters the surface, using PO methodology, the associated fields are transformed into surface currents and re-radiated to all observation points. Previously, the SBR method was known to pose difficulty in evaluating the wave diffraction at the edges and in the cavities of the model, but this shortcoming has been addressed using physical theory of diffraction (PTD) [15] and uniform theory of diffraction (UTD) [16].

Previously, research has been conducted addressing the accuracy of both SBR and MLFMM techniques. Many researchers have provided the comparative analysis of MLFMM, PO, and SBR method [17–19]. Some acceleration techniques have also been proposed for SBR [20–24]. Improvements in the SBR method, to incorporate different diffraction techniques, have also been suggested [15, 20]. In all of these studies however, only theoretical results are compared. There have been a few attempts to experimentally validate the RCS using basic shapes [25–27]. Very little data, if any, exist that provides a correlation of experimental measurements and approximate methods for complex structures such as an aircraft.

The purpose of this work is to provide an extensive correlation of SBR and MLFMM techniques for a fighter aircraft and subsequently compare it to the experimental results. This work would help benchmark the accuracy and applicability of two simulation techniques against the experimental measurement.

2 Mathematical background

2.1 Shooting and bouncing rays (SBR)

Consider a plane wave incident on a surface. The E-field is given by

$$\boldsymbol{E}_i = \left[h\hat{\theta}_i - v\hat{\varphi}_i\right]\mathrm{e}^{\mathrm{j}\boldsymbol{k}_i k_i \cdot \boldsymbol{r}} \tag{1}$$

where h and v are the amplitudes of the horizontally and vertically polarised components, respectively, and $\boldsymbol{k}_i$ is given by

$$\boldsymbol{k}_i = k_o\left(\hat{x}(\sin\theta_i\cos\varphi_i) + \hat{y}(\sin\theta_i\sin\varphi_i) + \hat{z}\cos\theta_i\right) \tag{2}$$

SBR incorporates principles of GO to trace the hit points on a surface. A wavefront is modelled as a bunch of parallel rays defined by the ray equation

$$\boldsymbol{R}(t) = \boldsymbol{O} + t\hat{D} \tag{3}$$

where t quantifies the phase of the incident field at the hit point, $\boldsymbol{O}$ is the origin vector carrying the reference point, and $\hat{D}$ is the unit vector in the direction of the ray.

Before going into the field computation, let us consider Fig. 1 where $\boldsymbol{R}_{\mathrm{inc}}$ is a ray incident at point P_1 on a surface S of the aircraft model and $\boldsymbol{R}_{\mathrm{ref}}$ is a reflected ray after bouncing from P_1. From Snell's law, the incident and reflected rays lie in the same plane and

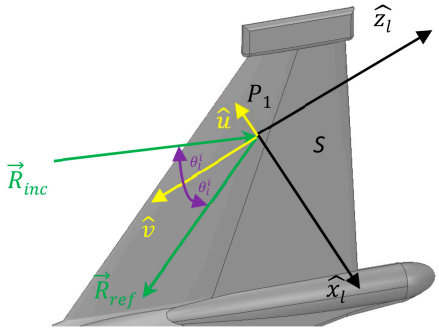

Fig. 1 *Local coordinate system with basis vectors $\hat{x}_l$, $\hat{y}_l$, $\hat{z}_l$, where $\hat{y}_l$ is inside the plane of the paper. According to Snell's law, the incident and reflected rays, $\boldsymbol{R}_{\text{inc}}$ and $\boldsymbol{R}_{\text{ref}}$, lie in the same plane, i.e. $\hat{y}_l\,\hat{z}_l$ plane*

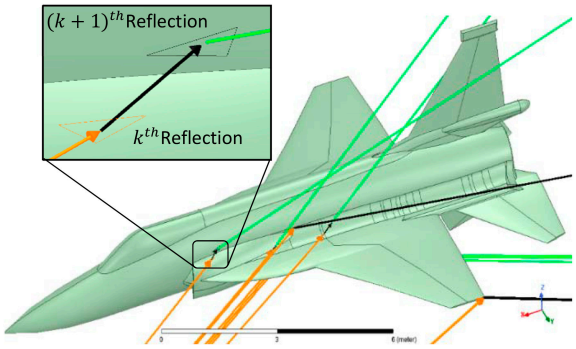

Fig. 2 *Ray tracing applied on the aircraft model under study. Multiple bounces are taken into account. The shape of the ray tube changes after every reflection, as accounted by the divergence factor (DF) and is shown in the inset*

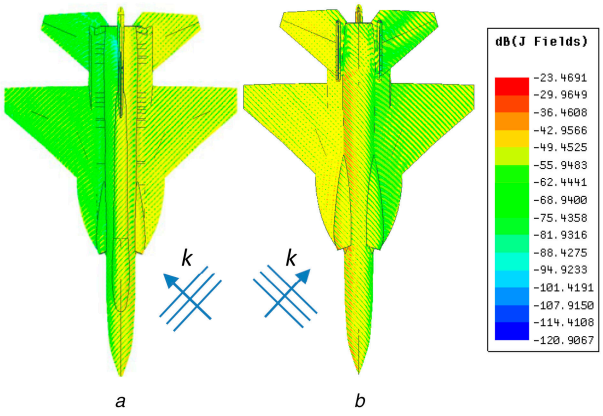

Fig. 3 *Surface current painted by an incident wave on our aircraft model* ***(a)*** Top view, ***(b)*** Bottom view

the angle of incidence, as measured from $\boldsymbol{R}_{\text{inc}}$ to the normal vector $\hat{v}$, is equal to the angle of reflection, as measured from $\hat{v}$ to $\boldsymbol{R}_{\text{ref}}$, if P_1 is the origin of a coordinate system where $\hat{x}_l$ is perpendicular to $\hat{v}$ while $\hat{u}$ is outside the plane of paper. The three basis vectors are as follows:

$$\hat{x}_l = \hat{u} \times \hat{v} \tag{4}$$

$$\hat{y}_l = -\hat{u} \tag{5}$$

$$\hat{z}_l = -\hat{v} \tag{6}$$

Using the above coordinate system, the elevation and azimuthal angles for the incident ray, θ_l^i and φ_l^i, are given by

$$\theta_l^i = \cos^{-1}(\boldsymbol{R}_{\text{inc}} \cdot \hat{v}) \tag{7}$$

$$\varphi_l^i = 0 \tag{8}$$

To compute the E-field associated with $\boldsymbol{R}_{\text{ref}}$, the incident E-field is decomposed into the transverse electric TE and transverse magnetic TM components because both the components realise that different reflection coefficients and θ_l^i and φ_l^i are translated to the global coordinate system.

Here, it is to be noted that in this technique, unlike PO, multiple reflections are taken into account. Once the ray is reflected from the surface, it moves on to a new surface and continues to reflect unless it reaches the exit aperture. During this entire cycle, the amplitude of the ray is to be tracked. The amplitude at $(k+1)$th reflection depends on the kth reflection, its reflection coefficient and divergence factor (DF):

$$\boldsymbol{E}(x_{k+1},\ y_{k+1}, z_{k+1}) = (\text{DF})_i \times \bar{\Gamma}_i \times E(x_k,\ y_k, z_k)\mathrm{e}^{-\mathrm{j}\varnothing} \tag{9}$$

where

$$\varnothing = k_o\left[(x_{k+1} - x_k)^2 + (y_{k+1} - y_k)^2 + (z_{k+1} - z_k)^2\right]^{1/2} \tag{10}$$

The term $(\text{DF})_i$ is a measure of the change in the shape of the ray tube in between kth and $(k+1)$th reflection as shown in Fig. 2.

Here, a differential part of a curved surface is assumed for which $\bar{\Gamma}_i$ is the planar reflection coefficient matrix. The derivation of DF for a curved surface is given in [28–30].

Equation (9) is used to find the E-field at the exit plane which induces a surface current that is computed using the following equation and is shown in Fig. 3:

$$\boldsymbol{M}_s = 2E(x_i,\ y_i, 0) \times \hat{z} \tag{11}$$

This surface current radiates to give rise to a backscattering field given by

$$\boldsymbol{E}_{\text{RCS}} = \frac{\mathrm{e}^{-\mathrm{j}k_o r}}{r}\left[\hat{\theta}_i A_\theta + \hat{\varphi}_i A_\varphi\right] \tag{12}$$

$$\begin{bmatrix} A_\theta \\ A_\varphi \end{bmatrix} = \frac{\mathrm{j}k_o}{2\pi}\iint \mathrm{e}^{\mathrm{j}k_o((\sin\theta_i\cos\varphi_i)x + (\sin\theta_i\sin\varphi_i)y)} \cdot \begin{bmatrix} E_x\cos\varphi_i + E_y\sin\varphi_i \\ (-E_x\sin\varphi_i + E_y\cos\varphi_i)\cos\theta_i \end{bmatrix}\mathrm{d}x\mathrm{d}y \tag{13}$$

The above integral is carried out to compute the contribution of each ray tube where E_x and E_y are the x and y components of the E-field on the exit aperture. Here, θ_i and φ_i are used because we are interested in monostatic RCS. The terms A_θ and A_φ are directly related to RCS at both vertical and horizontal polarisations. Plane wave assumption is applied to approximate the E-field within each ray tube on the exit aperture. It is to be noted that, so far, only specular reflections have been taken into account; however, in conjunction to the specular reflection, there are other phenomena, such as edge diffraction, that contribute to the RCS.

To quantify diffraction effects, diffraction coefficients are computed using UTD [16] which tends to generate additional rays to compensate for the diffraction in the shadow regions. In our simulations, we have considered the wedge angle $\alpha \leq 135°$. Fig. 4 shows the resulting wedges highlighted in thick yellow lines. To accurately model diffraction effects, in addition to UTD, we have also employed PTD with an approximation of 20 edge segments/wavelength.

2.2 Multi-level fast multipole method (MLFMM)

MLFMM is a well-established technique and is discussed briefly in this section. It is an acceleration method used by the MoMs [31]. The computational domain of the aircraft model is subdivided into cubes with different side lengths at each level (Fig. 5). The cubes at the lowest level are as small as 0.25λ.

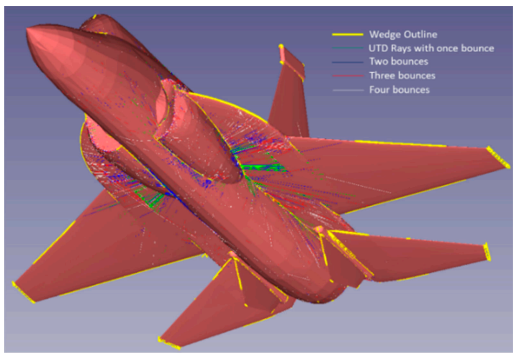

Fig. 4 *Wedge outline and UTD rays footprints that bounce off the CAD model*

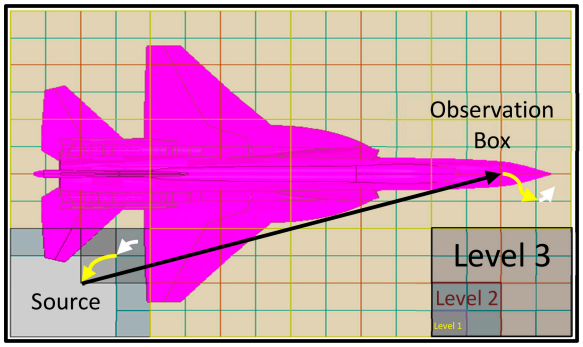

Fig. 5 *Hypothetical multi-levels for multipole expansion. The arrows show the up-sampling, translation, and down-sampling of fields*

The matrix of unknowns given by the system of linear equations, previously solved traditionally, is decomposed into a near-field and a far-field term:

$$Y = AX \tag{14}$$

$$Y = A_n X + A_f X \tag{15}$$

The near-field term A_n is computed at every box in level 1. The currents contained within the box are projected onto a multipole at the centre of each box. For every box in level 2, the multipole contribution due to its child boxes is computed, as shown by white arrows in Fig. 5. This procedure is cascaded to compute the multipoles at the highest level.

Fields are translated from one box (referred to as the source box) to another box (referred to as the observation box) lying in the far field of the source box. To aggregate the effect of every multipole on an observation box, addition theorem for Green's function is used. The fields at the lower level are computed by using the received fields at each observation box. This procedure is again cascaded to find the fields at the lowest level, and appropriate testing functions are used to verify. This is an iterative process and is summarised by an up-sampling U, translation T, and down-sampling D of fields:

$$A_f X_k = \mathrm{DTU} X_k \tag{16}$$

This operation, DTU, is applied on Green's function, and the convergence of the iterative process is accelerated by a preconditioner that is computed using the near-field term A_n (17):

3 RCS simulations

Monostatic RCS is computed using the SBR and MLFMM techniques at four operating frequencies, i.e. 0.5, 1, 1.5, and 2 GHz in vertical (VV) polarisation because most of the ground-based radars operate at these frequencies. The aircraft model was illuminated from a pitch angle of 0° in the yaw plane. The material of the aircraft model is taken as a perfect electric conductor (PEC).

All the simulations were conducted on the HP 2820 workstation incorporating 64 GB RAM and Intel Xeon processors with 16 logical CPUs, each having 2.1 GHz clock frequency. The overall computation time for each simulation is outlined in Table 1. As illustrated, with SBR, the computation time is considerably lower for the same geometry. This is due to the fact that SBR is a one-step solution that uses the less number of triangle intersections for the given size and frequency, and that these triangular elements almost remain constant even for higher frequency setups, whereas MLFMM is an iterative method that computes the residual error after every iteration and RCS is computed based on the specified convergence criterion. Furthermore, in MLFMM, the number of triangular mesh elements increases with higher frequency settings, thereby consuming more time and computational resources.

4 Model fabrication and testing

The aircraft model was built in CATIA v5. Fig. 6 shows the computer-aided design (CAD) of our fighter aircraft. The full-scale model has a wingspan of 9.48 m, total length of 14.93 m, and a height of 4.72 m. This model is scaled down to size 1:8 as necessitated by the size of the anechoic chamber for RCS measurement. Scaling down the model implies that the analysis frequency should be scaled up by the same scaling factor, whereas permittivity and permeability are unaffected by the scaling. Therefore, measurements were carried out at 4, 8, 12, and 16 GHz at the same permittivity and permeability values.

The selection of materials is important in model fabrication because of the weight and size constraints of the test section. The model was fabricated using Ebaboard 60-1 (also known as chemical wood). It is a synthetic, post-cured chemical wood with an excellent strength-to-weight ratio and machining properties. The wood is brown-red in colour and has a density of 600 kg/m^3. The aircraft model was fabricated using a 5-axis computer numerical control machine which used two carving spindle along the contours of the model by utilising two additional rotational axes of motion. The model is an exact match to the original CAD design of the aircraft. The experimental evaluation and far-field testing of the aircraft was done in a compact RCS test chamber. The test chamber has dimensions of 2 m × 2 m × 4 m, and it can carry a maximum weight of 60 kg. The fabricated model weighs 24 kg. The surface of the model was coated with CHO-SHIELD® 4900 conductive coating which emulates the exact conductive parameters and dielectric properties of PEC.

Fig. 7 shows the experimental setup for RCS measurement. The test chamber is a dual reflector setup with a reflector antenna of length 15 ft, width 8 ft, and height 6 ft with the frequency range of up to 20 GHz. Inside the test chamber, the supporting structure on which the aircraft model is mounted is made of Styrofoam which has a very low RCS [5, 7]. The walls of the test chamber are also shielded with broadband RF absorbers, giving an ideal environment for far-field measurement without EM noise and interference. The elevation plane is kept constant at 0°, whereas the azimuth is rotated for a complete 360°. The test was performed for the VV polarisation of the required frequencies.

5 Results and discussion

The comparison chart in Fig. 8 shows the mean RCS in the azimuth plane for simulated versus the measured results. It can be seen that, at 0.5 GHz, the differences between SBR and MLFMM techniques versus experimental results are well within the 3 dB limit. The difference is even less at 1 and 1.5 GHz, whereas the maximum deviation is observed at 2 GHz which corresponds to a scaled-up frequency of 16 GHz. At such a high frequency, the incident wavelength becomes small enough to highlight the minute details, and hence, the fabrication and measurement tolerances become noticeably large and affect the comparison to simulated results. This effect can be seen by the mean absolute error taken with respect to the measured RCS, as shown in Table 2.

Fig. 9 shows the superimposed rectangular plots for the simulated and experimental results corresponding to each test frequency. The independent variable is the azimuthal angle with an

Table 1 Number of mesh elements and simulation time comparison between MLFMM and SBR

Technique	xxx	Frequency and polarisation			
		0.5 GHz VV	1G Hz VV	1.5 GHz VV	2 GHz VV
MLFMM	number of mesh elements (triangles)	278,892	391,398	763,132	868,346
	simulation time (hours)	9	14	18	22
SBR	number of mesh elements (triangles)	161,052	162,634	161,136	162,706
	simulation time (hours)	0.57	0.58	0.83	0.8

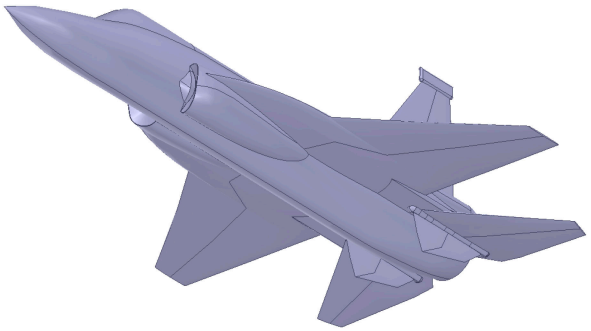

Fig. 6 *CAD model of a fighter aircraft*

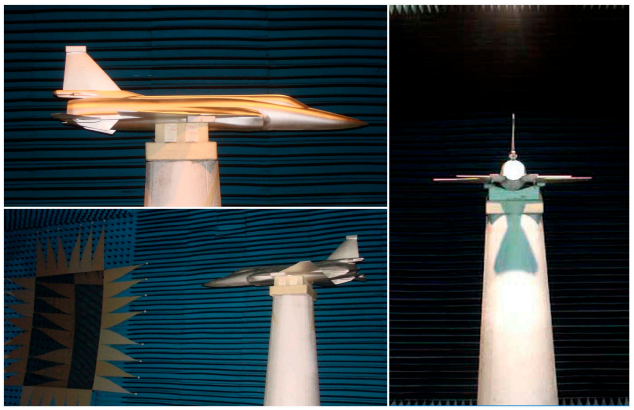

Fig. 7 *Experimental setup for RCS far-field testing*

angular resolution of $\Delta \varnothing = 1°$ where the nose of the aircraft model is at $\varnothing = 0°$. On the other hand, the dependent variable is the monostatic RCS in dBsm for VV polarisation. Results demonstrate that the RCS pattern computed using the low-fidelity SBR method qualitatively follows similar traces as that of the high-fidelity MLFMM technique. The quantitative variation between the two results is primarily due to the fact that SBR is an approximate methodology employing ray tube tracing for calculations in which some of the launched rays are refracted to the far-field without being accounted for RCS contribution. This offset can also be attributed to the fact that only those rays are contributing towards the RCS which bounce off the target for a maximum number of four times.

From the above discussion, it can be concluded that, since the SBR method can provide fast and accurate qualitative RCS results, it can be incorporated into a modelling and simulation environment where thousands of design iterations are required. However, MLFMM, being a high fidelity and computationally intensive method, is still required to capture the subtle geometric variations and to get an accurate quantitative RCS analysis for a finalised aircraft geometry. The slight deviation in simulated results can be attributed to imperfections in model fabrication, material properties, and the non-ideal environment of the anechoic chamber, but it is within the allowable limits. Overall, the results established the fact that the SBR technique gives accurate results much similar to the MLFMM in the simulated environment in far less computation time. This reiterates the claim that for the fast design optimisation of aircraft models in terms of RCS, the SBR method provides a quick result for CAD models in the design environment with high, close to measured result, accuracy.

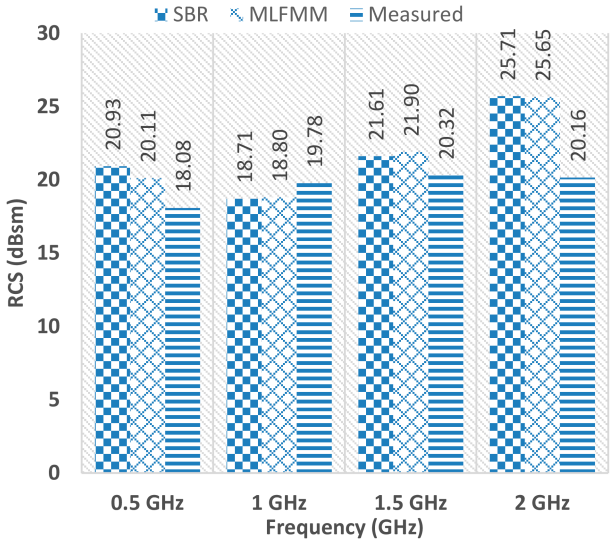

Fig. 8 *Mean RCS (dBsm) comparison between MLFMM, SBR, and experimental results*

Table 2 Mean Absolute Error of simulation techniques with experimental data for various frequencies in VV polarisation

Technique	Frequency and polarisation			
	0.5 GHz VV	1 GHz VV	1.5 GHz VV	2 GHz VV
MLFMM	4.48	5.66	6	6.56
SBR	4.24	5.85	5.19	6.65

6 Conclusion

This paper presents the fidelity analysis of SBR and MLFMM for the RCS computation of a fighter aircraft. For validation, the simulated results of both techniques are compared with the measured data of the same aircraft. The results indicate that a simple SBR technique, notwithstanding its much lower simulation time, provides reasonably accurate results of RCS for the complex geometry such as a fighter aircraft. This is not to undermine the importance of the high-fidelity MLFMM technique which may be employed at the cost of higher computational power and more simulation time if precise values of RCS and effects of subtle variations in design parameters are desired. The advantage of SBR is that such simplistic, fast, and accurate method can be integrated in a modelling and simulation environment.

7 Acknowledgments

The authors would like to appreciate the tireless efforts of Mr. Ali Zahid Bhatty, Department of Mechatronics Engineering, Air University, Islamabad, Pakistan for designing the CAD model used in this research.

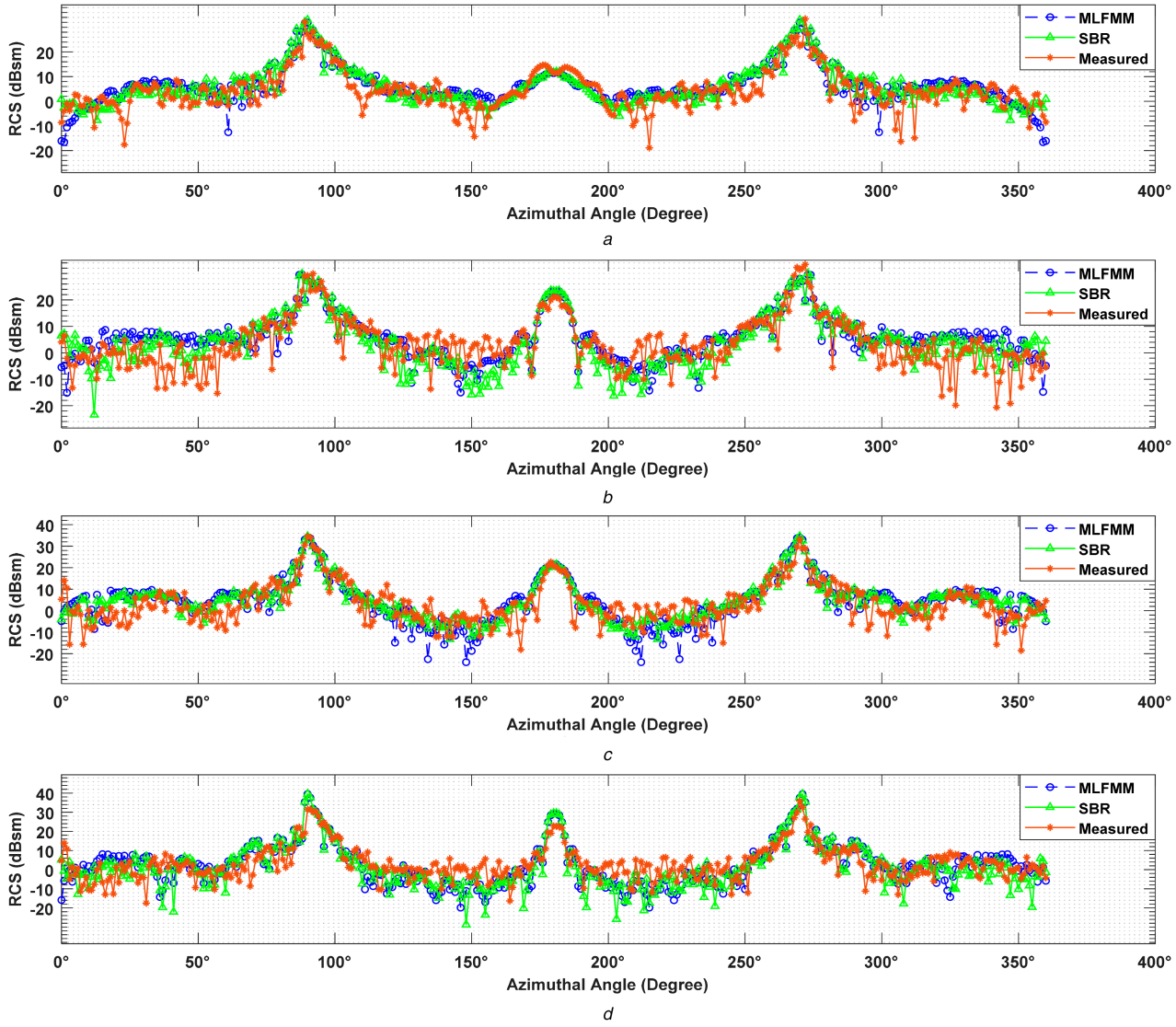

Fig. 9 *MLFMM vs SBR vs measured results for various frequencies in VV polarisation*
(a) 0.5 GHz, ***(b)*** 1 GHz, ***(c)*** 1.5 GHz, ***(d)*** 2 GHz

8 References

[1] Chusov, A., Protopopova, A, Lysenko, A.: 'Parallel computer simulation of radio waves propagation over large urban areas and irregular terrain'. 9th Int. Conf. on Computing, Communication and Networking Technologies (ICCCNT), Bengaluru, India, 2018

[2] Lin, Z., Zhao, X., Zhang, Y., *et al.*: 'Performance of a massively parallel higher-order method of moments code using thousands of CPUs'. Int. Conf. on Electromagnetics in Advanced Applications (ICEAA), Cartagena, Colombia, 2018

[3] Linghu, L., Wu, J., Huang, B., *et al.*: 'GPU-accelerated massively parallel computation of electromagnetic scattering of a time-evolving oceanic surface generation', *J. Sel. Top. Appl. Earth Obs. Remote Sens.*, 2018, **11**, (8), pp. 2752–2762

[4] Mei, X., Zhang, Y., Lin, H.: 'A new efficient hybrid SBR/MoM technique for scattering analysis of complex large structures'. Int. Conf. on Computational Electromagnetics (ICCEM), Hong Kong, 2015

[5] Knott, E.F.: '*Radar cross section measurements*' (Springer Science & Business Media, Berlin, Germany, 2012)

[6] Ahmad, M.H., Kasilingam, D.P.: 'Spectral domain fast multipole method for solving integral equations of electromagnetic wave scattering', *Prog. Electromagn. Res.*, 2019, **80**, pp. 121–131

[7] Oswald, N., Monismith, D.R.: 'Radar cross sections of objects with simulated defects using the parallel FDTD method'. IEEE Symp. on Electromagnetic Compatibility, Signal Integrity and Power Integrity (EMC, SI & PI), Long Beach, CA, USA, 2018

[8] Li, J., Pan, Y., Guo, L., *et al.*: 'A bii-iterative model electromagnetic scattering from a ship floating on sea surface'. 12th Int. Symp. on Antennas, Propagation and EM Theory (ISAPE), Hangzhou, China, 2018

[9] Ling, H., Chou, R.-C., Lee, S.-W.: 'Shooting and bouncing rays: calculating the RCS of an arbitrarily shaped cavity', *IEEE Trans. Antennas Propag.*, 1989, **37**, (2), pp. 194–205

[10] Schick, M., Jakobus, U., Schoeman, M., *et al.*: 'Extended solution methods in FEKO to solve actual antenna simulation problems: accelerated MoM and windscreen antenna modelling'. Proc. of the 5th European Conf. on Antennas and Propagation (EUCAP), Rome, Italy, 2011

[11] Ma, L., Nie, Z., Hu, J., *et al.*: 'Combined MLFMA-ACA algorithm application to scattering problems with complex and fine structure'. Asia Pacific Microwave Conf., Singapore, 2009

[12] Zan, G., Guo, L., Liu, S., *et al.*: 'Scattering characteristics of thehe multi-corner reflector based on SBR method'. 12th Int. Symp. on Antennas, Propagation and EM Theory (ISAPE), Hangzhou, China, 2018

[13] Taygur, M.M., Sukharevsky, I.O., Eibert, T.F.: 'Investigation of massive MIMO scenarios involving rooftop propagation by bidirectional rayay-tracing', *Prog. Electromagn. Res.*, 2019, **91**, pp. 129–142

[14] Xu, W., Guo, L., Chai, S.: 'Improved SBR method for backward scattering of ship target under shallow sea background'. 12th Int. Symp. on Antennas, Propagation and EM Theory (ISAPE), Hangzhou, China, 2018

[15] Jeng, S.-K.: 'Near-field scattering by physical theory of diffraction and shooting and bouncing rays', *IEEE Trans. Antennas Propag.*, 1998, **46**, (4), pp. 551–558

[16] Mc Namara, D.A., Pistorius, C.W.I., Malherbe, J.A.G.: '*Introduction to the uniform theory of diffraction*' (Artech House, Norwood, MA, USA, 1990)

[17] Smit, J.C., Burger, E.H., Cilliers, J.E.: 'Comparison of MLFMM, PO and SBR for RCS investigations in radar applications'. IET Int. Conf. on Radar Systems, Glasgow, UK, 2012

[18] Li, Z., *et al.*: 'Electromagnetic scattering characteristics of PEC targets in the terahertz regime', *IEEE Antennas Propag. Mag.*, 2009, **51**, (1), pp. 39–50

[19] Liu, Z.-L., Wang, C.-F.: 'Shooting and bouncing ray and physical optics for predicting the EM scattering of coated PEC objects'. IEEE Asia-Pacific Conf. on Antennas and Propagation (APCAP), Singapore, 2012

[20] Tao, Y., Lin, H., Bao, H.: 'GPU-based shooting and bouncing ray method for fast RCS prediction', *IEEE Trans. Antennas Propag.*, 2010, **58**, (2), pp. 494–502

[21] Gao, P.C., Tao, Y.B., Lin, H.: 'Fast RCS prediction using multiresolution shooting and bouncing ray method on the GPU', *Prog. Electromagn. Res.*, 2010, **107**, pp. 187–202

[22] Gao, P.C., Liang, Z.C., Gao, W..: 'Kd-tree based shooting and bouncing ray method for fast computation of near field scattering'. PIERS Proc., Guangzhou, China, 2014
[23] Suk, S., Seo, T.-I., Park, H.-S., *et al.*: 'Multiresolution grid algorithm in the SBR and its application to the RCS calculation', *Microw. Opt. Technol. Lett.*, 2001, **29**, pp. 394–397
[24] Jin, K.-S., Suh, T.-I., Suk, S-H., *et al.*: 'Fast ray tracing using a space-division algorithm for RCS prediction', *J. Electromagn. Waves Appl.*, 2006, **20**, (1), pp. 119–126
[25] Ross, R.: 'Radar cross section of rectangular flat plates as a function of aspect angle', *IEEE Trans. Antennas Propag.*, 1966, **14**, (3), pp. 329–335
[26] Taflove, A., Umashankar, K.R.: 'Review of FD-TD numerical modeling of electromagnetic wave scattering and radar cross section'. Proc. of the IEEE, 1989, pp. 682–699
[27] Paquay, M., Iriate, J.-C., Ederra, I., *et al.*: 'Thin AMC structure for radar cross-section reduction', *IEEE Trans. Antennas Propag.*, 2007, **55**, (12), pp. 3630–3638
[28] Deschamps, G.A.: 'Ray techniques in electromagnetics', *Proc. IEEE*, 1972, **60**, pp. 1022–1035
[29] Lee, S.W., Cramer, P., Woo, K., *et al.*: 'Diffraction by an arbitrary subreflector: GTD solution', *IEEE Trans. Antenna Propag.*, 1979, **AP-27**, pp. 305–316
[30] Lee, S.W., Sheshadri, M.S., Jamnejad, V., *et al.*: 'Reflection at a curved dielectric interface: geometrical optics solution', *IEEE Trans. Microwave Theory Tech.*, 1982, **MTT-30**, pp. 12–19
[31] Song, J, Lu, C.-C., Chew, W.C.: 'Multilevel fast multipole algorithm for electromagnetic scattering by large complex objects', *IEEE Trans. Antennas Propag.*, 1997, **45**, (10), pp. 1488–1493